



1 **Fracturing and crystal plastic behavior of garnet under seismic stress in the**  
2 **dry lower continental crust (Musgrave Ranges, Central Australia)**

---

3  
4

5 Friedrich Hawemann<sup>1\*</sup>, Neil Mancktelow<sup>1</sup>, Sebastian Wex<sup>1</sup>, Giorgio Pennacchioni<sup>2</sup>, Alfredo  
6 Camacho<sup>3</sup>

7 1) Department of Earth Sciences, ETH Zurich, CH8092 Zurich, Switzerland

8 2) Department of Geosciences, University of Padova, Padova, Italy

9 3) Department of Geological Sciences, University of Manitoba, Winnipeg, Manitoba, R3T  
10 2N2, Canada

11 \* corresponding author [friedrich.hawemann@erdw.ethz.ch](mailto:friedrich.hawemann@erdw.ethz.ch)

12

13 **Highlights**

- 14 • garnet deformed by fracturing and crystal-plasticity under dry lower crustal conditions
- 15 • Ca-diffusion profiles indicate multiple generations of fracturing
- 16 • diffusion is promoted along zones of higher dislocation density
- 17 • fracturing indicates transient high-stress (seismic) events in the lower continental  
18 crust

19 **Abstract**

20 Garnet is a high strength mineral compared to other common minerals such as quartz and  
21 feldspar in the felsic crust. In felsic mylonites, garnet typically occurs as porphyroclasts that



22 mostly evade deformation, except under relatively high temperature conditions. The  
23 microstructure of granulite facies garnet in felsic lower-crustal rocks of the Musgrave Ranges  
24 (Central Australia) records both fracturing and crystal-plastic deformation. Granulite facies  
25 metamorphism at ~ 1200 Ma generally dehydrated the rocks and produced mm-sized garnets  
26 in peraluminous gneisses. A later ~ 550 Ma overprint under sub-eclogitic conditions (600-700  
27 °C, 1.1-1.3 GPa) developed shear zones and with abundant pseudotachylyte, coeval with the  
28 neocrystallization of fine-grained, high-calcium garnet. The granulitic fractured garnet  
29 porphyroclasts in mylonites show high calcium content along rims and fractures. However, in  
30 certain cases, these rims are narrower than equivalent rims along original grain boundaries,  
31 indicating contemporaneous diffusion and fracturing of garnet. The fractured garnets exhibit  
32 internal crystal-plastic deformation, that coincide with areas of enhanced diffusion, usually  
33 along zones of crystal lattice distortions and dislocation walls and by subgrain rotation  
34 recrystallization. Fracturing of garnet under dry lower crustal conditions, in an otherwise  
35 viscously flowing matrix, requires transient high differential stress, most likely related to  
36 seismic rupture, consistent with the coeval development of abundant pseudotachylyte.

37

#### 38 **Keywords**

39 Garnet, Fracture, Crystal-Plasticity, Dry Lower Continental Crust, Pseudotachylyte, Seismicity

#### 40 **1 Introduction**

41 A fundamental problem in geology is the limited preservation of processes in the rock record.  
42 This is especially the case for transient events, like earthquakes, traces of which are hardly  
43 preserved due to later reworking. The best indicators for seismicity in the rock record are



44 pseudotachylytes (Sibson, 1975; Toy et al., 2011), although not every seismic event produces  
45 frictional melts and, once formed, ductile creep or later brittle fracturing may erase most  
46 traces (Sibson and Toy, 2006; Kirkpatrick and Rowe, 2013).

47 Garnet is stable in many metamorphic rocks over a large part of the pressure-temperature  
48 space, is commonly preserved, and is suitable for a range of geothermobarometers and  
49 geochronometers and their combination for geospeedometry (Lasaga, 1983; Caddick et al.,  
50 2010; Baxter and Scherer, 2013). Being a high strength mineral (Karato et al., 1995; Wang and  
51 Ji, 1999), both brittle and crystal plastic deformation are rarely observed in garnet when  
52 compared to the common matrix minerals of the crust, such as quartz and feldspar. Dalziel  
53 and Bailey (1968) interpreted elongate garnets in a high grade mylonites as the result of  
54 crystal plastic behavior. Advancements since then in electron microscopy, and especially EBSD  
55 (electron backscatter diffraction), have allowed detailed investigation of garnet textures  
56 (Kunze et al., 1993; Prior et al., 2000, 2002).

57 Experimental deformation of garnet indicates that differential stresses on the order of a few  
58 GPa are required to produce shear fractures (Wang and Ji, 1999), and that the onset of ductile  
59 crystal plastic behavior only occurs at temperatures above 850 °C (Karato et al., 1995; Wang  
60 and Ji, 1999). The observation of fractured garnets in natural samples may therefore be linked  
61 to seismic stresses, as suggested by Austrheim et al. (1996), who described fracturing of  
62 garnets during pseudotachylyte formation and fluid-assisted eclogitization of granulites.  
63 Trepmann and Stöckhert (2002) also interpreted the microstructure of fractured and offset  
64 garnets as evidence for syn-seismic loading and post-seismic creep. In addition, Austrheim et  
65 al. (2017) also associated brittle and crystal-plastic behavior of garnets with lower crustal  
66 seismic events. Papa et al. (2018) interpreted similar deep-seated dilatant fracturing of garnet



67 immediately adjacent to pseudotachylyte to be related to thermal shock due to frictional  
68 heating rather than to damage associated with propagation of the seismic rupture.

69 Here we present a study of garnet microstructures from lower crustal rocks of the Musgrave  
70 Block in Australia, which:

- 71 (1) illustrates the close association between brittle and ductile deformation of garnet  
72 under well-established pressure-temperature conditions;
- 73 (2) infers deformation mechanisms from the observed microstructure;
- 74 (3) explores the close link between deformation and diffusion in garnet;
- 75 (4) complements other independent observations indicating transient high stresses in the  
76 lower crust.

77

## 78 **2 Geological setting**

### 79 **2.1 Regional geology**

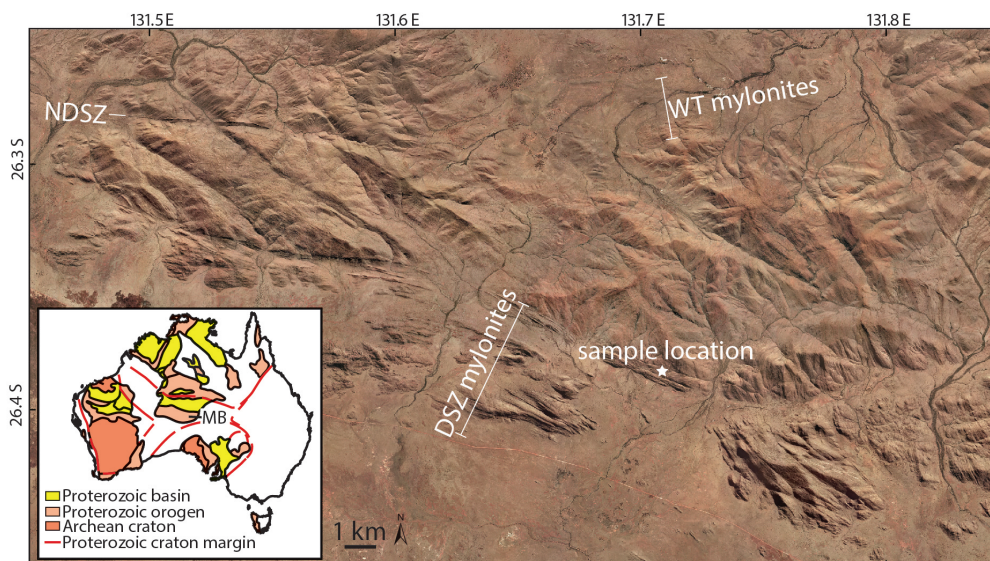
80 The Musgrave Block is located in an intraplate position close to the center of the Australian  
81 continent (inset Fig. 1). Amalgamation of the different cratonic blocks took place during the  
82 Musgravian Orogeny (1120-1200 Ma), which pervasively overprinted ca. 1550 Ma gneisses  
83 (Gray, 1978; Camacho and Fanning, 1995). The Petermann Orogeny (~550 Ma) produced a  
84 series of crustal-scale fault zones, most prominently the Woodroffe Thrust and the Mann  
85 Fault (Collerson et al., 1972; Major, 1973; Bell, 1978; Camacho and Fanning, 1995; Raimondo  
86 et al., 2010; Wex et al., 2017, 2018, 2019). The south-dipping Woodroffe Thrust has a top-to-  
87 the-north sense of shear, and juxtaposes the Fregon Subdomain in the south (hanging wall)  
88 against the Mulga Park Subdomain in the north (footwall). During the Musgravian Orogeny,



89 the Mulga Park Subdomain attained amphibolite facies conditions while the Fregon  
90 Subdomain reached granulite facies (Camacho and Fanning, 1995; Scrimgeour et al., 1999;  
91 Scrimgeour and Close, 1999), and depleted the rocks of OH-bearing minerals (Wex et al.,  
92 2018; Hawemann et al., 2018).

93 The Woodroffe Thrust hosts one of the largest occurrences of pseudotachylyte worldwide  
94 (Camacho et al., 1995), but all larger scale shear zones in the hanging wall also show abundant  
95 pseudotachylyte that developed under lower crustal conditions (Camacho, 1997; Hawemann  
96 et al., 2018). Deformation in the Fregon Subdomain associated with the Petermann Orogeny  
97 is concentrated along the sub-eclogitic (~650 °C, 1.2 GPa) Davenport Shear Zone and the  
98 North Davenport Shear Zone (Fig. 1), with little discernible overprint of the earlier granulites  
99 in between (Camacho et al., 1997). The Davenport Shear Zone is a WNW-ESE-striking, strike-  
100 slip zone, with a near horizontal stretching lineation. Deformation inside the Davenport Shear  
101 Zone itself is heterogeneous and strongly localized (Hawemann et al., 2019).

102



103

Figure 1: Airborne imagery of the study area with sample location (26.3849 S, 131.7067 E) in the Davenport Shear Zone (DSZ). NDSZ = North Davenport Shear Zone, WT = Woodroffe Thrust. Image from the Department of Primary Industries and Regions, South Australia (PIRSA), 2012. Inset: Location of the Musgrave Block (MB) in between the Australian Cratons. Modified after Evins et al. (2010)

104

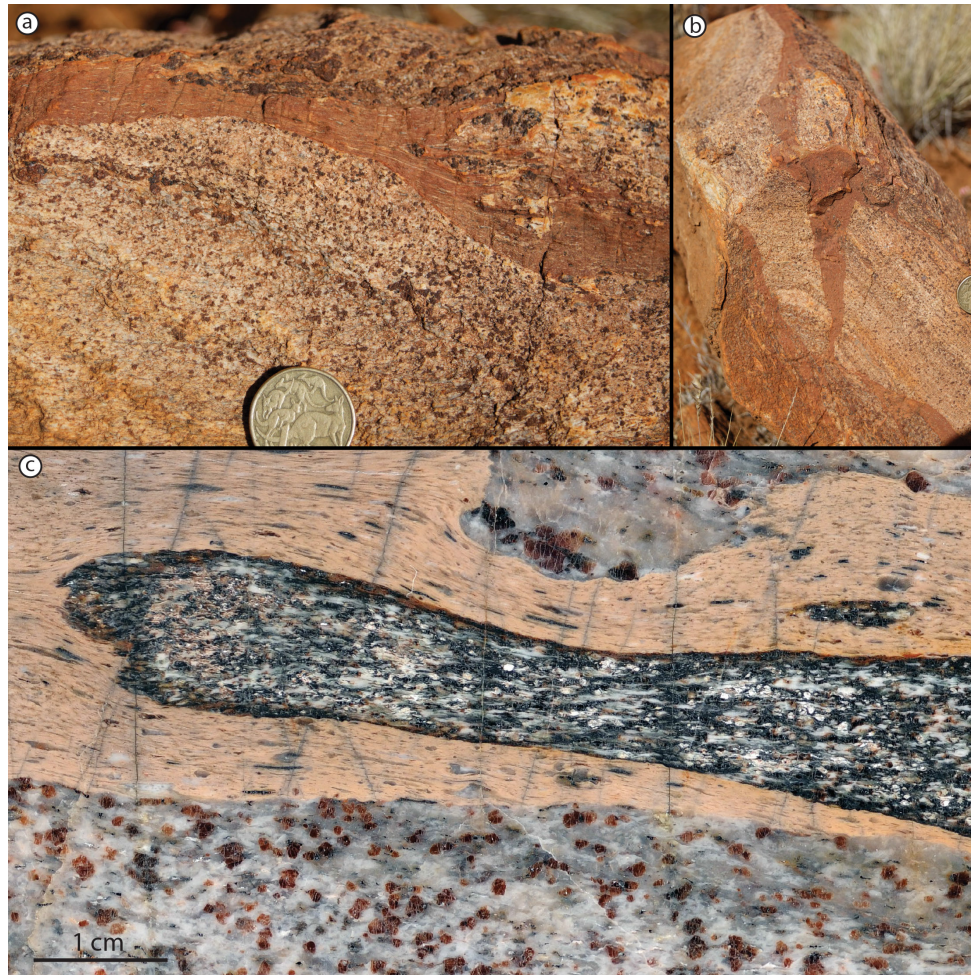
## 105 2.2 Sample description

106 Fractured garnet is ubiquitous in the Fregon Subdomain and is not exclusively found in  
107 association with pseudotachylyte veins. However, this study focuses on a representative  
108 outcrop for which field relationships, metamorphic, and deformation conditions have been  
109 well established (F68, Hawemann et al., 2018; 26.3849 S, 131.7067 E). This outcrop consists  
110 of a quartzo-feldspathic mylonite, with millimeter-sized, granulite facies garnets, that  
111 includes multiple pseudotachylyte veins and breccias. Pseudotachylytes in the studied  
112 outcrop are sheared, as indicated by elongated clasts (Fig. 2a, c), and show the same  
113 stretching lineation as the host mylonite. The original discordant relationship to the host  
114 foliation is still preserved and cuts perpendicular to the stretching lineation (Fig. 2b).



115 The syn-mylonitic assemblage associated to the Petermann overprint of felsic granulites is  
116  $Qz+Kfs+Pl+Gt+Bt+Ky+Ilm+Rt$  (mineral abbreviations following Whitney and Evans, 2010), and  
117 is similar to that of the associated sheared pseudotachylyte ( $Qz+Kfs+Pl+Gt+Bt+Ky+Rt$ ). The  
118 fine-grained garnet growing within the pseudotachylyte gives the rock its caramel-color in  
119 macroscopic images (Fig. 2 Fractured garnets are clearly recognizable in polished hand  
120 specimens (Fig. 2c) and are very apparent in thin section (Fig. 3). The metamorphic conditions  
121 during shearing of this pseudotachylyte are estimated at  $\sim 600$  °C and  $\sim 1.1$  GPa (Fig. 7 of  
122 Hawemann et al, 2018).

123



124

Figure 2: Sheared pseudotachylyte in a view orthogonal to the foliation of host felsic mylonite, and perpendicular (a) and parallel (b) to the stretching lineation. c) Polished hand specimen of a sheared pseudotachylyte breccia with the caramel-colored foliated pseudotachylyte matrix including elongated clasts and an elongate fragment of mafic granulite. The host rock shows millimeter-sized garnets with fractures.

125

### 126 3 Garnet microstructure and compositional variation

#### 127 3.1 Optical microstructure

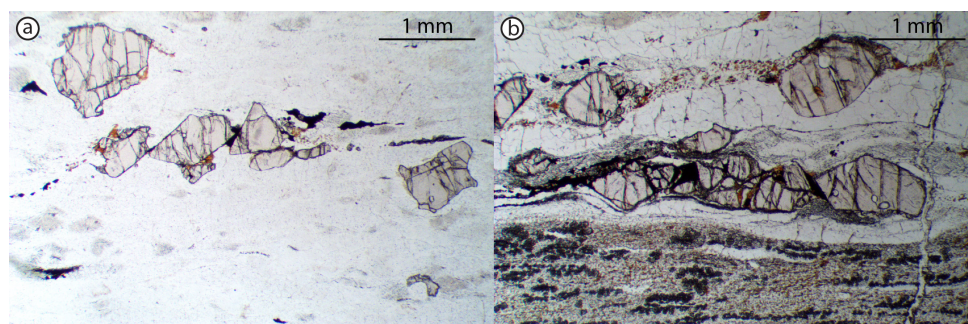
128 Granulite facies garnet porphyroclasts in Musgravian peraluminous gneisses mylonitized  
129 during the Petermann Orogeny are almost invariably fractured, irrespective of their proximity





130 to pseudotachylyte (Fig. 3). Large garnet porphyroclasts (>1 mm) are typically slightly  
131 elongated with their long axis parallel to the foliation, which is attributed at least partially to  
132 resorption. Fractures in garnets often show offsets in the order of a few 100  $\mu\text{m}$ . It is not  
133 possible to determine whether these offsets are primarily due to the initial shear fracture or  
134 result from subsequent sliding during ongoing ductile shear. Moreover, no consistent sense  
135 of shear can be derived from the offsets (Fig. 3a, b). These discrete fractures are sub-planar,  
136 commonly have a consistent orientation at a moderate angle to the foliation, and locally occur  
137 in conjugate sets (Fig. 3b). Wide fractures are filled with biotite, kyanite and quartz (Fig. 4b).  
138 An apparent late generation of unfilled dilatant fractures is oriented perpendicular to both  
139 the foliation and stretching lineation (Fig. 3b). Garnet porphyroclasts commonly contain rutile  
140 exsolution lamellae and inclusions of monazite and kyanite (Fig. A1). The latter are present as  
141 aggregates with an overall prismatic shape, possibly representing pseudomorphs after  
142 sillimanite (Camacho and Fitzgerald, 2010).

143



144

*Figure 3: Thin section photomicrographs in plane polarized light of fractured garnets away from pseudotachylyte (a), and close to sheared and recrystallized pseudotachylyte in the lower part of the figure (b). The dark trails of grains elongated in the foliation of the sheared pseudotachylyte are small new garnets.*

145

146

147



148        3.2 Analytical techniques

149        Quantitative mineral compositions were measured with a JEOL JXA-8200 electron probe  
150        micro-analyzer (EPMA), equipped with a tungsten filament, at the Institute of Geochemistry  
151        and Petrology at ETH Zurich (Switzerland). Natural standards were used for quantification,  
152        and, when available, natural garnet standards were preferred. To reach a spatial resolution  
153        of about 1  $\mu\text{m}$ , an acceleration voltage of 10 kV was set (Fig. 8 in Hofer and Brey, 2007).  
154        Elemental maps were acquired using energy wavelength-dispersive spectrometers in parallel  
155        for calcium, to increase the signal-to-noise ratio. Backscatter electron images (BSE), energy-  
156        dispersive spectrometry (EDS) and electron backscatter diffraction (EBSD) mapping was  
157        carried out on a Quanta 200F field emission gun (FEG) scanning electron microscope at the  
158        ScopeM (Scientific Center for Optical and Electron Microscopy, ETH Zurich). EBSD maps were  
159        collected with an acceleration voltage of 20 kV, a sample tilt of 70° and a working distance of  
160        15 mm. Data were post-processed using chemical indexing with the software OIM 7 by EDAX.  
161        When necessary, three different clean-up techniques were used: neighbor confidence index  
162        correlation, neighbor orientation correlation and grain dilation. Point and map analyses, as  
163        well as BSE images, were combined for correlation with optical microscope images in a QGIS-  
164        project (Open Source Geospatial foundation). Two lamellae were cut with a focused ion beam  
165        (FIB) for transmission electron microscopy (TEM). The microscope used for TEM is a Tecnai  
166        F30 with a FEG source operated at 300 kV and equipped with a Gatan 794 MultiScan CCD  
167        (ScopeM, ETH Zurich).

168        3.3 Compositional gradients

169        Granulite facies garnet has a homogeneous composition of  $X_{\text{Alm}} 0.54$ ,  $X_{\text{Py}} 0.40$ ,  $X_{\text{Grs}} 0.03$ ,  $X_{\text{Sps}}$   
170        0.03, whereas garnet neocrystallized during the Petermann Orogeny is more Ca-rich ( $X_{\text{Alm}}$

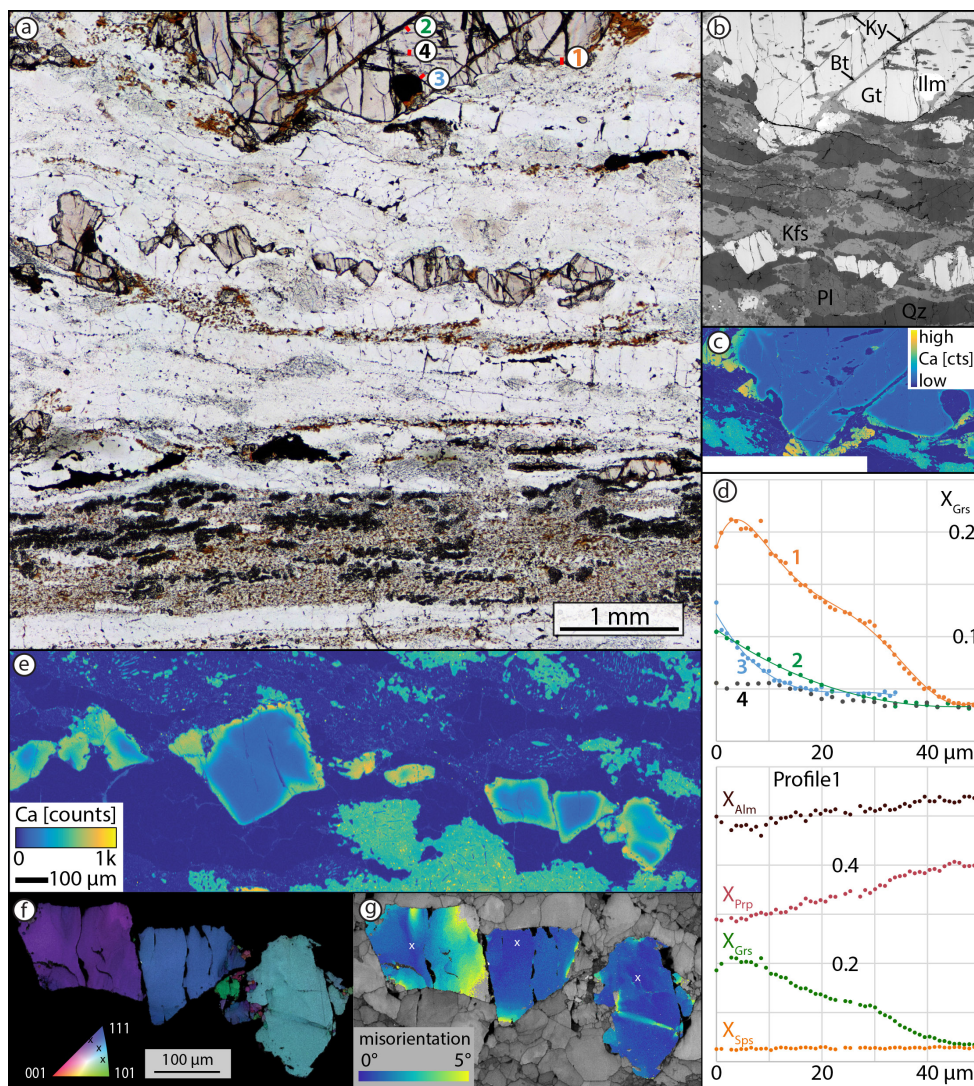


171 0.48,  $X_{\text{Pyp}}$  0.28,  $X_{\text{Grs}}$  0.22,  $X_{\text{SpS}}$  0.02). Grain boundaries of granulite facies garnet and fractures  
172 are decorated with a Ca-enriched rim, 20 to 40  $\mu\text{m}$  wide (Fig. 4c). The enrichment is mostly  
173 concentric, also affects resorbed areas of the garnet and is therefore most likely the result of  
174 diffusion (Camacho et al., 2009). Neocrystallized garnet is present where the grain boundary  
175 is in contact with, or close to, plagioclase. The outermost rim of remnant garnet has the same  
176 composition as the neocrystallized garnet (Fig. 4d, profile 1). The granulitic plagioclase is  
177 partially transformed to a more Na-rich plagioclase with needle shaped inclusions of kyanite  
178 (bottom of Fig. 4e). This reaction provides Ca for the observed diffusion into garnet (Camacho  
179 et al., 2009).

180 Along fractures across the porphyroclasts, the Ca enrichment is narrower than along the grain  
181 boundaries and the grossular component only reaches up to about  $X_{\text{Grs}}$  0.1 (Fig. 4d, profile 2).  
182 Compositional gradients are also present around inclusions in garnet connected to the outer  
183 garnet boundary providing evidence of Ca diffusion along grain boundaries (right part of Fig.  
184 4c, profile 3 in Fig 4d). Profile 4 (Fig. 4d) was measured next to a kyanite inclusion: the  
185 diffusion length is still comparable to those of profiles 1-3, but Ca concentrations are much  
186 lower. Ca probably diffused along fractures (invisible in the plane of the thin section) towards  
187 the inclusion. In summary, the diffusion length at the original grain boundaries is maximized  
188 where in contact with plagioclase, and otherwise constant at about 20  $\mu\text{m}$  width. However,  
189 variations in diffusion lengths do occur around garnet fragments, without any correlation with  
190 the proximity to plagioclase, although the exact relationship in the third dimension is  
191 unknown. Surfaces with limited diffusion can often be identified as fracture surfaces, which  
192 were exposed to diffusion for a shorter time than original grain boundaries (Fig. 4e). Fractures  
193 oriented perpendicular to the foliation and stretching lineation lack any signs of diffusion and  
194 are therefore interpreted as later stage dilatant fractures.



195 Some garnets display more complicated compositional patterns, with zones  $>100\ \mu\text{m}$  of Ca  
196 enrichment into the porphyroclast's interior, which are not associated with fractures (e.g.  
197 the garnet fragment on the far right in Figure 4e). EBSD-analysis highlights that the three  
198 fragments in the right part of Figure 4e most likely originated from the same grain, as they  
199 share a common rotation axis (Fig. 4f). The colors in the inverse pole figure map are not solid,  
200 reflecting slight variations of orientation within the crystal. Furthermore, the image quality  
201 map shows areas of suppressed Kikuchi patterns (grey value) suggestive of higher dislocation  
202 density and therefore possible subgrain boundaries (Fig. 4f). The misorientation angle map  
203 (Fig. 4g) reveals a complex pattern of varying crystal orientation (all within the order of  $5^\circ$ ) in  
204 the fragments, with very distributed zones connected to the edges of the crystal, triangular-  
205 shaped zones of misorientation (upper left of Fig. 4g), and discrete zones (lower right of Fig.  
206 4g). The discrete zones of misorientation, about  $5\ \mu\text{m}$  wide, correlate well with the Ca-  
207 enriched zones (compare Fig. 4e, f, garnet fragment on the right).



208

Figure 4: a) Plane polarized light image of thin section with fractured garnets and a pseudotachylyte vein in the lower part of the image. b) BSE image of the upper area of (a), with same scale as (a). c) EPMA X-ray map for Ca reveals the thin diffusion rim along grain boundaries, fractures, and neocrystallized garnet (euhedral, orange). d) Grossular component profiles indicated on (a) (Profile lines are not to scale for the sake of visibility); and compositional profiles for four garnet end-members in profile 1. e) EPMA X-ray map for Ca for the garnet fragments in the center of (a). Note the uneven colors in the plagioclase and the blue kyanite needles. f) Inverse pole figure map with superimposed image quality map for garnet fragments shows common rotation pole. g) Misorientation map relative to reference point for each fragment reveals internal lattice distortions.

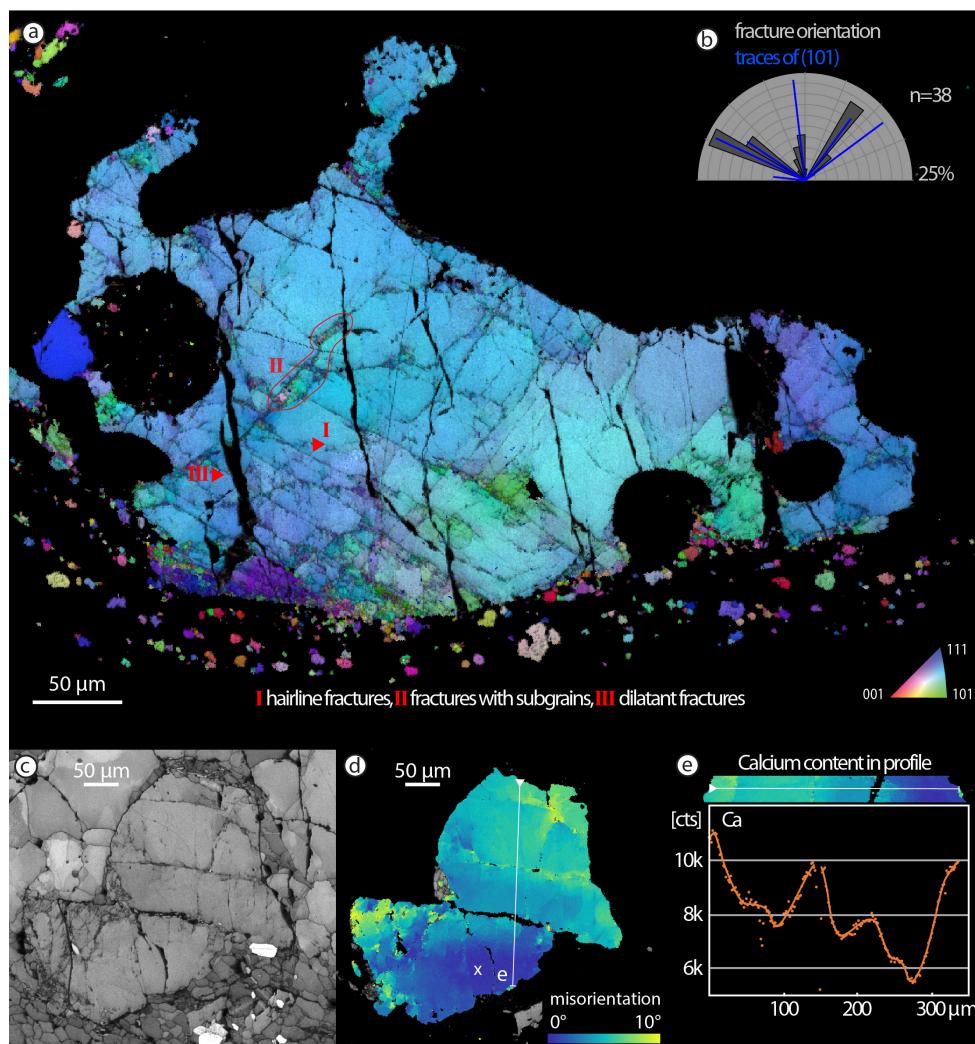
209



210 3.4 Texture of deformed garnets

211 Two to three orientations of fractures are generally present in a single garnet crystal and  
212 coincide with the trace of the (101)-plane derived from EBSD data (Fig. 5a, b). Fracture set (I)  
213 in the example of Figure 5a is often associated with a relative rotation of both sides, as visible  
214 from the difference in color. In the lower part of the grain, where the fracture density is very  
215 high, subgrains are present. The subgrain spatial density increases towards the original grain  
216 boundary and some subgrains are “eroded” by ductile shearing and strung out along the  
217 foliation. This demonstrates that ductile shearing outlasted subgrain formation and  
218 fracturing. Subgrains of less than 10  $\mu\text{m}$  in size formed in the fracture plane (II in Fig. 5a). The  
219 fractures described above are all crosscut by dilatant fractures (set III in Fig. 5a), oriented  
220 perpendicular to the stretching lineation and foliation, which do not show any associated  
221 distortion of the crystal lattice.

222 The garnet porphyroclast of Figure 5c shows a central fracture as well as a set of two other  
223 parallel fractures. The central fracture is the only one with significant offset and is filled with  
224 kyanite and quartz. This fracture displays misorientations of more than  $5^\circ$  towards the right-  
225 hand side of the scan, but none towards the left-hand side. In the lower left corner of the  
226 fragment, subgrains are observed with misorientations, relative to the average orientation,  
227 typically in the range of  $10^\circ$ . Misorientation axes are often parallel to (111) and (101). The  
228 lowermost fragment shows a wide zone of progressive rotation. The chemical profile in Figure  
229 5e shows the highest Ca counts towards the boundaries of the porphyroclasts and, internally,  
230 towards two fractures. The larger fracture with apparent offset of the two garnet fragments  
231 exhibits a less efficient calcium diffusion when compared to the tight fracture with introduced  
232 lattice distortion.



233

Figure 5: a) Inverse pole figure map of fractured garnet with three dominant orientations of fractures. b) Rose diagram correlating traced fracture orientations and (101)-planes for garnet in (a). c) Image quality map of a fragmented garnet with subgrains. d) Misorientation plot (with respect to the point marked with the white x) shows long wavelength bending in the lower fragment and distortion in the crystal lattice induced by a fracture in the upper fragment. e) EDS-calcium counts for the profile marked as a thin white line in (d).

234

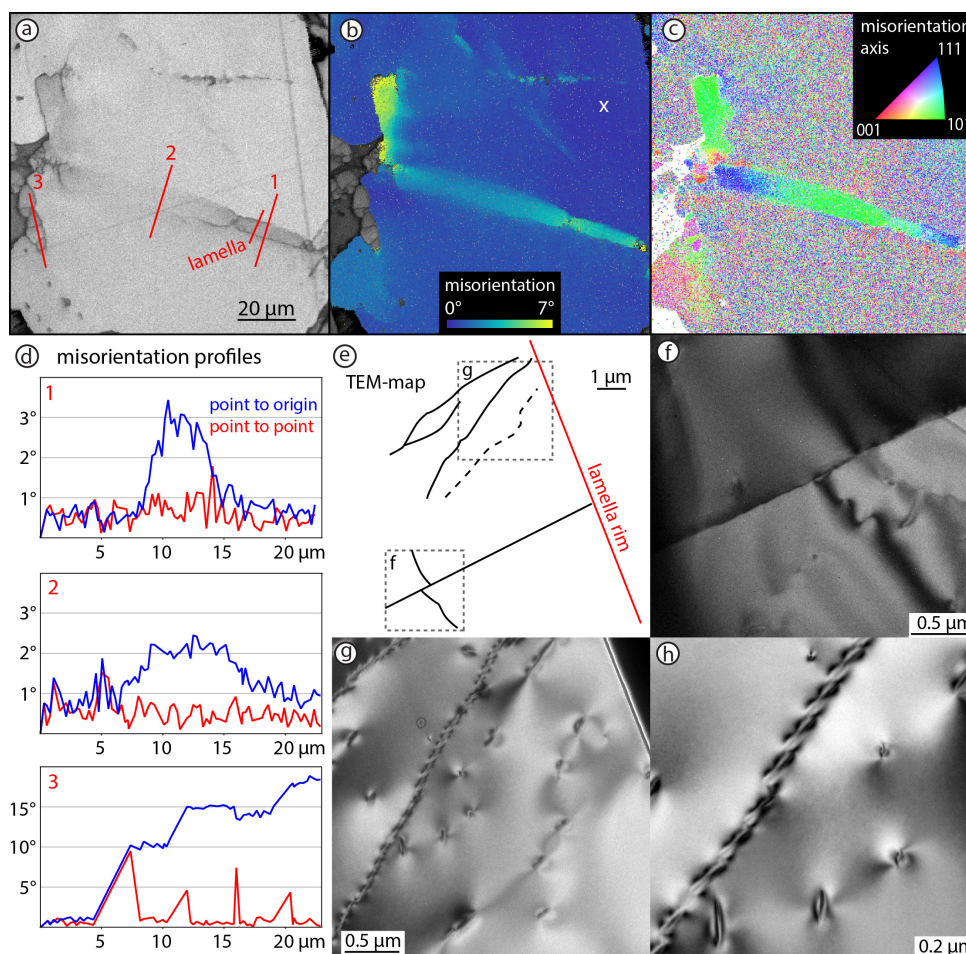
235



236 3.5 TEM investigations

237 The garnet fragment of Figure 4g was further investigated using TEM, as it includes a narrow  
238 zone of misorientation without fractures and is therefore suitable for preparation of FIB-  
239 lamellae. As visible in Figure 6a (around profile 1), the image quality map shows a well-defined  
240 narrow, darker grey band, possibly indicating high dislocation density. The zone is even more  
241 evident in the misorientation plot (Fig. 6b) and changes from about 5  $\mu\text{m}$  wide, with discrete  
242 boundaries to the right, to a wider (> 10  $\mu\text{m}$ ) band towards the left of the image. In the upper  
243 left part of the image, a subgrain boundary with > 5° misorientation transitions into a zone of  
244 gradual misorientation. The misorientation axis is consistently parallel to (101) with minor  
245 rotation around (111) (Fig. 6c, Fig. A2). Misorientation profiles reveal a slight asymmetry  
246 within the narrow band, where the lower boundary appears to be sharper. Misorientation  
247 changes more gradually within the wider portion of the misorientation band. Locally,  
248 subgrains developed with discrete boundaries, documenting a misorientation of usually  
249 around 5-10° (profile 3 in Fig. 6d). The FIB-lamella was cut across the narrow band of  
250 misorientations (Fig. 6e). The lower boundary corresponds to a narrow discrete zone, without  
251 visible dislocations (Fig. 6f). The upper boundary is marked by a series of dislocation walls and  
252 only a few free dislocations are visible, which are often organized in arrays (Fig. 6g, h). The  
253 existence of dislocation walls indicates recovery by dislocation climb.





254

Figure 6: a) Image quality map of the garnet fragment (compare Fig. 4f) with darker zones that can be interpreted as areas of high dislocation density and location of the FIB-lamella. b) Misorientation plot with respect to the reference point (marked with the white x) shows a discrete zone of misorientation, which has discrete boundaries in the right part of the image, but is more distributed towards the left. c) Misorientation axis plot with respect to the average orientation of the grain shows a consistent rotation around the (101) and (111) axes. For pole figure plots, see Fig. A2. d) Misorientation profiles indicated in a), for (1) the narrow zone, (2) the more distributed zone and (3) for subgrains. e) Overview sketch of the FIB-lamella used for TEM-analysis for correlation with the EBSD data. f) Sharp contrast boundary in the lower part of the lamella. g) Two dislocation walls with a few free dislocations, which are partly linking up parallel to the dislocation walls. h) Detail of the center of (g)

255

256



257 **4 Discussion**

258 Garnets in this study show evidence for both brittle and ductile deformation under relatively  
259 low temperatures of about 600 °C, as inferred from synchronous diffusion and ductile  
260 shearing of pseudotachylyte (Hawemann et al, 2018). This is well below the experimentally  
261 determined values for the onset of crystal-plastic deformation of garnet (>850 °C; Wang and  
262 Ji, 1999). In contrast to experiments, many natural examples (Vollbrecht et al., 2006;  
263 Bestmann et al., 2008; Austrheim et al., 2017) indicate crystal plasticity of garnet at lower  
264 temperatures between 650 °C and 700 °C, challenging the reliability of extrapolation of  
265 experimental data to natural conditions.

266 The presence of microstructures and -textures consistent with dislocation climb and recovery,  
267 as well as subgrain rotation, in garnet at around 600 °C is in agreement with previous  
268 studies (Bestmann et al., 2008; Massey et al., 2011). No evidence for grain boundary sliding is  
269 observed, since subgrains show rotation around a specific crystallographic axis. Rotation  
270 around (111) and (101) is in accordance with the slip systems described by Voegelé et al.  
271 (1998).

272 Multiple generations of overprinting fractures with different orientation demonstrate  
273 repeated fracturing events. Tensile fractures do not show any induced lattice distortion or  
274 diffusion and therefore occurred after the temperature was too low for diffusion (Camacho  
275 et al., 2009), possibly during exhumation (compare Prior, 1993 and Ji et al., 1997).

276 In contrast to the observations of Austrheim et al. (2017) and Papa et al. (2018) from other  
277 examples in the deep continental crust, no “explosive fracturing” or “shattering” of garnet is  
278 observed in relict porphyroclasts immediately adjacent to pseudotachylyte. The fractures  
279 described here are generally planar and often consistently oriented, in some cases showing



280 single and conjugate shear offsets. Fractured garnet is still present in samples without  
281 pseudotachylyte, where the nearest pseudotachylyte is possibly many meters or more away.  
282 Fracturing in this case cannot be related to thermal shock (Papa et al., 2018), but must reflect  
283 differential stresses high enough to cause brittle garnet failure.

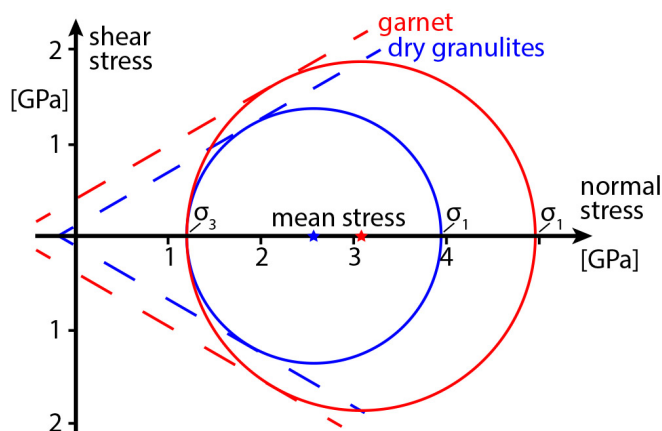
284 The narrower Ca diffusion profiles on some fractures relative to garnet rims and crosscutting  
285 relationships suggest that fracturing was recurrent under sub-eclogite facies metamorphic  
286 conditions, as also indicated by the occasional presence of kyanite in some of some fractures.  
287 The presence of kyanite needles and the absence of zoisite/clinozoisite or epidote, as a  
288 breakdown product of plagioclase during sub-eclogitic metamorphism (Fig. 3b), indicate  
289 relatively dry lower crustal conditions (Hawemann et al., 2018). According to Wayte et al.  
290 (1989), this indicates a water activity of  $< 0.004$ , calculated for rocks of comparable  
291 composition and P-T conditions. However, new biotite did form in dilatant fractures across  
292 relict garnet, so conditions were probably not strictly anhydrous. The sheared and  
293 recrystallized pseudotachylyte developed a similar synkinematic assemblage as the host  
294 mylonite, demonstrating that there is also no marked partitioning of water into the frictional  
295 melt, which implies little free or bound water available in the original source rock (e.g. Wex  
296 et al., 2018). The effect of pore-fluid pressure on the effective confining pressure must  
297 therefore have been negligible.

298 As reported in Hawemann et al. (2019), the dynamically recrystallized quartz grain size and  
299 microstructure in the host rock mylonites indicates that long-term flow stresses were not  
300 particularly high, on the order of less than 10 MPa. The ambient pressure of ca. 1.1-1.2 GPa  
301 determined for the host rocks should therefore be close to the lithostatic value (Mancktelow,  
302 2008). Figure 7 shows a simple linear plot of the Mohr-Coulomb failure criterion for an angle



303 of internal friction of  $30^\circ$  (coefficient  $\mu = 0.6$ ), a lithostatic load of 1.2 GPa, and no pore fluid  
304 pressure. This plot is only qualitative, since the angle of internal friction could decrease  
305 towards higher pressure. However, the summary of experimental results in Byerlee (1978)  
306 indicates that there may be little change at least up to pressures similar to those considered  
307 here. It follows that the differential stress for fracture initiation must have been of the same  
308 order as the confining pressure (Fig. 7). As discussed in detail in Hawemann et al. (2019), such  
309 high differential stresses, leading to garnet fracture and the development of abundant  
310 pseudotachylyte, can only have been transient and presumably related to repeated short-  
311 term seismic events in the lower continental crust. The lack of shattered garnet adjacent to  
312 pseudotachylyte in these samples may reflect drier conditions relative to those in the Bergen  
313 Arc (Austrheim et al., 2017) and Mont Mary (Papa et al., 2018). The samples studied could  
314 therefore represent one end-member of the lower continental crust, where deformation  
315 occurs without the initial presence or influx of free water during fracturing and subsequent  
316 crystal-plastic deformation.

317



318



*Figure 7: Mohr circles for fracturing of dry granulites and garnet at 1.2 GPa lithostatic load*

319

## 320 **5 Conclusions**

321 In dry lower continental crust deformed under conditions of ca. 600 °C and 1.1 GPa, garnet  
322 shows both single and conjugate sets of shear fractures, fractures with associated subgrains  
323 and induced lattice damage around fractures, subgrain formation without fracturing, and  
324 late-stage dilatant fractures. Most of these fractures show a strong crystallographic control,  
325 with fracturing preferentially occurring along the (101) planes of garnet. Dynamic  
326 recrystallization is evident from inferred subgrain rotation recrystallization and recovery is  
327 manifested by the presence of dislocation walls. The observed microstructures of garnets are  
328 interpreted to record transient high stresses during deep seismic events in the lower crustal  
329 Fregon Subdomain, which is also indicated by the abundant occurrence of pseudotachylyte  
330 developed under similar lower crustal conditions and, possibly, by the variability of  
331 recrystallized quartz grain sizes including values down to a few micrometers (Hawemann et  
332 al. 2009b). The studied example represents one end-member of lower continental crustal  
333 behavior where, because of earlier metamorphic dehydration and the intracratonic position  
334 well removed from the plate margin, rocks were initially dry and water was not introduced  
335 during fracturing and crystal-plastic deformation.

336

## 337 **Acknowledgements**

338 We gratefully acknowledge permission granted to work on the Anangu Pitjantjatjara  
339 Yankunytjatjara Lands (APY) to carry out our field work in the area. The Northern Territory  
340 Geological Survey (NTGS) and Basil Tikoff (Department of Geoscience, University of



341 Wisconsin) are thanked for their logistical support and the Nicolle family of Mulga Park station  
342 for their hospitality. The Scientific Center for Optical and Electron Microscopy (ScopeM)  
343 provided the facilities for the scanning electron microscopy work, and help by Karsten Kunze,  
344 Luiz Morales and Fabian Gramm is especially acknowledged. Luca Menegon is thanked for  
345 his review of the first author's doctoral thesis. This project was financed by the Swiss National  
346 Science Foundation (SNF) grant 200021\_146745 and by the University of Padova  
347 (BIRD175145/17: The geological record of deep earthquakes: the association  
348 pseudotachylite-mylonite).

349

#### 350 **Data Availability**

351 All data used in this paper can be accessed through the depository of the Open Science  
352 Framework here: <https://osf.io/yrzgh/>

353

#### 354 **References**

- 355 Austrheim, H., Erambert, M. and Boundy, T. M.: Garnets recording deep crustal earthquakes, *Earth*  
356 *and Planetary Science Letters*, 139(1–2), 223–238, doi:10.1016/0012-821X(95)00232-2, 1996.
- 357 Austrheim, H., Dunkel, K. G., Plümper, O., Ildefonse, B., Liu, Y. and Jamtveit, B.: Fragmentation of  
358 wall rock garnets during deep crustal earthquakes, *Science Advances*, 3(2), e1602067,  
359 doi:10.1126/sciadv.1602067, 2017.
- 360 Baxter, E. F. and Scherer, E. E.: Garnet Geochronology: Timekeeper of Tectonometamorphic  
361 Processes, *Elements*, 9(6), 433–438, doi:10.2113/gselements.9.6.433, 2013.
- 362 Bell, T. H.: Progressive deformation and reorientation of fold axes in a ductile mylonite zone: the  
363 Woodroffe thrust, *Tectonophysics*, 44(1), 285–320, 1978.
- 364 Bestmann, M., Habler, G., Heidelberg, F. and Thöni, M.: Dynamic recrystallization of garnet and  
365 related diffusion processes, *Journal of Structural Geology*, 30(6), 777–790,  
366 doi:10.1016/j.jsg.2008.02.007, 2008.



- 367 Caddick, M. J., Konopasek, J. and Thompson, A. B.: Preservation of Garnet Growth Zoning and the  
368 Duration of Prograde Metamorphism, *Journal of Petrology*, 51(11), 2327–2347,  
369 doi:10.1093/petrology/egq059, 2010.
- 370 Camacho, A. and Fanning, C. M.: Some isotopic constraints on the evolution of the granulite and  
371 upper amphibolite facies terranes in the eastern Musgrave Block, central Australia, *Precambrian  
372 Research*, 71(1), 155–181, 1995.
- 373 Camacho, A. and Fitz Gerald, J. D.: Misidentification of oxide phases and of twinned kyanite:  
374 implications for inferred P-T histories of the Musgrave Block, central Australia, *Journal of the Virtual  
375 Explorer*, 35, doi:10.3809/jvirtex.2011.00275, 2010.
- 376 Camacho, A., Vernon, R. H. and Fitz Gerald, J. D.: Large volumes of anhydrous pseudotachylyte in the  
377 Woodroffe Thrust, eastern Musgrave Ranges, Australia, *Journal of Structural Geology*, 17(3), 371–  
378 383, 1995.
- 379 Camacho, A., Compston, W., McCulloch, M. and McDougall, I.: Timing and exhumation of eclogite  
380 facies shear zones, Musgrave Block, central Australia, *J. metamorphic Geol.*, 15, 735–751, 1997.
- 381 Camacho, A., Yang, P. and Frederiksen, A.: Constraints from diffusion profiles on the duration of  
382 high-strain deformation in thickened crust, *Geology*, 37(8), 755–758, 2009.
- 383 Collerson, K. D., Oliver, R. L. and Rutland, R. W. R.: An example of structural and metamorphic  
384 relationships in the Musgrave orogenic belt, central Australia, *Journal of the Geological Society of  
385 Australia*, 18(4), 379–393, doi:10.1080/00167617208728776, 1972.
- 386 Dalziel, I. W. D. and Bailey, S. W.: Deformed garnets in a mylonitic rock from the Grenville Front and  
387 their tectonic significance, *American Journal of Science*, 266(7), 542–562, doi:10.2475/ajs.266.7.542,  
388 1968.
- 389 Evins, P. M., Smithies, R. H., Howard, H. M., Kirkland, C. L., Wingate, M. T. D. and Bodorkos, S.:  
390 Redefining the Giles Event within the setting of the 1120–1020 Ma Ngaanyatjarra Rift, West  
391 Musgrave Province, Central Australia, *Geological Society of Western Australia, East Perth, W.A.*,  
392 2010.
- 393 Gray, C. M.: Geochronology of granulite-facies gneisses in the western Musgrave Block, Central  
394 Australia, *Journal of the Geological Society of Australia*, 25(7–8), 403–414,  
395 doi:10.1080/00167617808729050, 1978.
- 396 Hawemann, F., Mancktelow, N. S., Wex, S., Camacho, A. and Pennacchioni, G.: Pseudotachylyte as  
397 field evidence for lower-crustal earthquakes during the intracontinental Petermann Orogeny  
398 (Musgrave Block, Central Australia), *Solid Earth*, 9(3), 629–648, doi:10.5194/se-9-629-2018, 2018.
- 399 Hawemann, F., Mancktelow, N. S., Pennacchioni, G., Wex, S. and Camacho, A.: Weak and slow,  
400 strong and fast: How shear zones evolve in a dry continental crust (Musgrave Ranges, Central  
401 Australia), *Journal of Geophysical Research: Solid Earth*, doi:10.1029/2018JB016559, 2019.
- 402 Hofer, H. E. and Brey, G. P.: The iron oxidation state of garnet by electron microprobe: Its  
403 determination with the flank method combined with major-element analysis, *American  
404 Mineralogist*, 92(5–6), 873–885, doi:10.2138/am.2007.2390, 2007.
- 405 Ji, S., Zhao, P. and Saruwatari, K.: Fracturing of garnet crystals in anisotropic metamorphic rocks  
406 during uplift, *Journal of Structural Geology*, 19(5), 603–620, 1997.



- 407 Karato, S., Wang, Z., Liu, B. and Fujino, K.: Plastic deformation of garnets: systematics and  
408 implications for the rheology of the mantle transition zone, *Earth and Planetary Science Letters*,  
409 130(1–4), 13–30, 1995.
- 410 Kirkpatrick, J. D. and Rowe, C. D.: Disappearing ink: How pseudotachylytes are lost from the rock  
411 record, *Journal of Structural Geology*, 52, 183–198, doi:10.1016/j.jsg.2013.03.003, 2013.
- 412 Kunze, K., Wright, S. I., Adams, B. L. and Dingley, D. J.: Advances in automatic EBSD single orientation  
413 measurements, *Texture, Stress, and Microstructure*, 20(1–4), 41–54, 1993.
- 414 Lasaga, A. C.: Geospeedometry: an extension of geothermometry, in *Kinetics and equilibrium in  
415 mineral reactions*, pp. 81–114, Springer. [online] Available from:  
416 [http://link.springer.com/chapter/10.1007/978-1-4612-5587-1\\_3](http://link.springer.com/chapter/10.1007/978-1-4612-5587-1_3) (Accessed 28 May 2017), 1983.
- 417 Major, R. B.: *Explanatory Notes for the Woodroffe 1: 250 000 Geological Map SG/52-12 (1st  
418 ed.)*. Adelaide, Australia: Geological Survey of South Australia, 1973.
- 419 Massey, M. A., Prior, D. J. and Moecher, D. P.: Microstructure and crystallographic preferred  
420 orientation of polycrystalline microgarnet aggregates developed during progressive creep, recovery,  
421 and grain boundary sliding, *Journal of Structural Geology*, 33(4), 713–730,  
422 doi:10.1016/j.jsg.2010.12.009, 2011.
- 423 Papa, S., Pennacchioni, G., Angel, R. J. and Faccenda, M.: The fate of garnet during (deep-seated)  
424 coseismic frictional heating: The role of thermal shock, *Geology*, 46(5), 471–474,  
425 doi:10.1130/G40077.1, 2018.
- 426 Prior, D. J.: Sub-critical fracture and associated retrogression of garnet during mylonitic deformation,  
427 *Contributions to Mineralogy and Petrology*, 113(4), 545–556, doi:10.1007/BF00698322, 1993.
- 428 Prior, D. J., Wheeler, J., Brenker, F. E., Harte, B. and Matthews, M.: Crystal plasticity of natural  
429 garnet: New microstructural evidence, *Geology*, 28(11), 1003, doi:10.1130/0091-  
430 7613(2000)28<1003:CPONGN>2.0.CO;2, 2000.
- 431 Prior, D. J., Wheeler, J., Peruzzo, L., Spiess, R. and Storey, C.: Some garnet microstructures: an  
432 illustration of the potential of orientation maps and misorientation analysis in microstructural  
433 studies, *Journal of Structural Geology*, 24(6–7), 999–1011, doi:10.1016/S0191-8141(01)00087-6,  
434 2002.
- 435 Raimondo, T., Collins, A. S., Hand, M., Walker-Hallam, A., Smithies, R. H., Evins, P. M. and Howard, H.  
436 M.: The anatomy of a deep intracontinental orogen, *Tectonics*, 29(4), n/a-n/a,  
437 doi:10.1029/2009TC002504, 2010.
- 438 Sibson, R. H.: Generation of pseudotachylyte by ancient seismic faulting, *Geophysical Journal  
439 International*, 43(3), 775–794, 1975.
- 440 Sibson, R. H. and Toy, V. G.: The habitat of fault-generated pseudotachylyte: Presence vs. absence of  
441 friction-melt, in *Geophysical Monograph Series*, vol. 170, edited by R. Abercrombie, A. McGarr, H.  
442 Kanamori, and G. Di Toro, pp. 153–166, American Geophysical Union, Washington, D. C. [online]  
443 Available from: <http://www.agu.org/books/gm/v170/170GM16/170GM16.shtml> (Accessed 21  
444 January 2014), 2006.

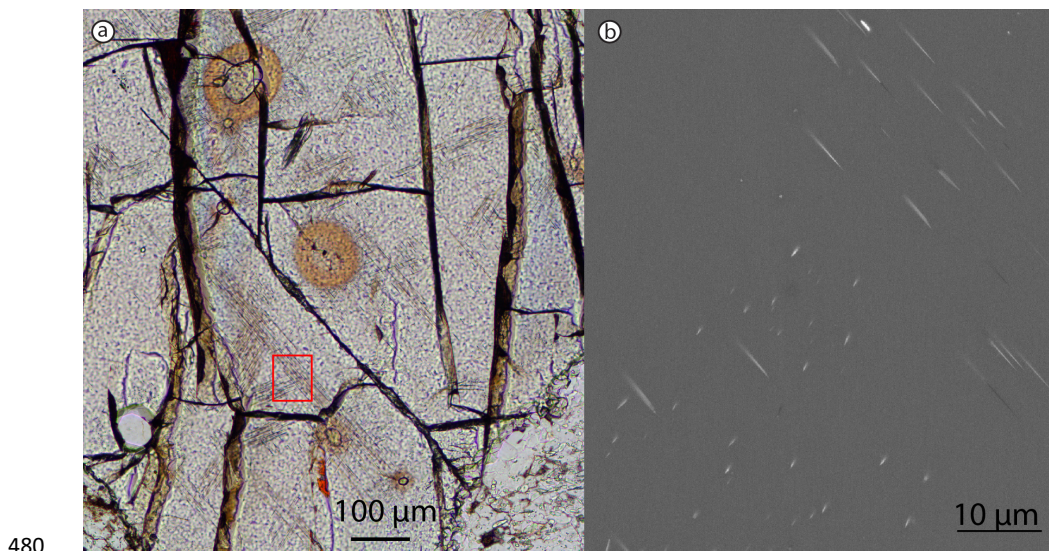




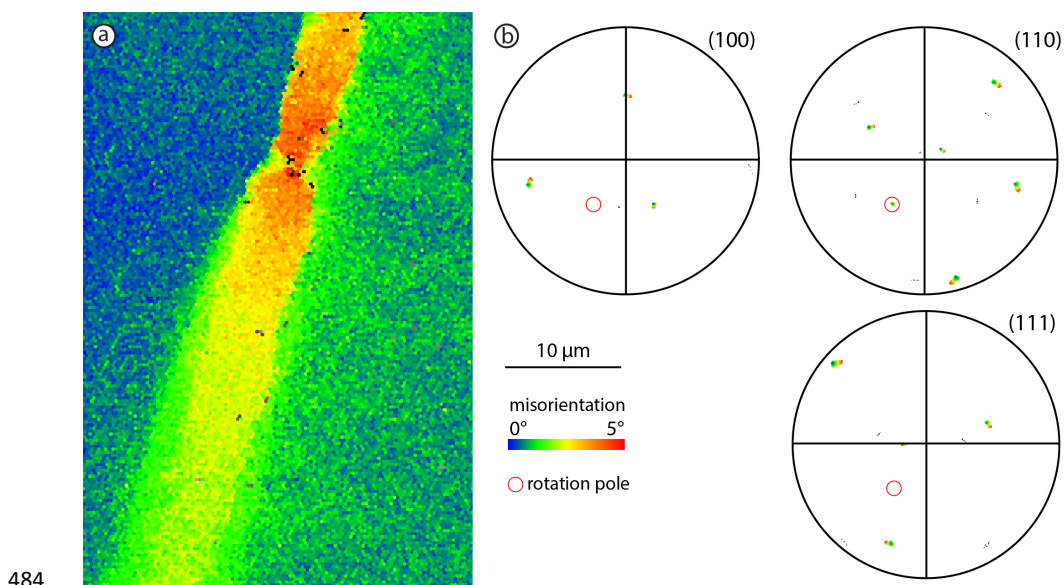
- 445 Toy, V. G., Ritchie, S. and Sibson, R. H.: Diverse habitats of pseudotachylytes in the Alpine Fault Zone  
446 and relationships to current seismicity, *Geological Society, London, Special Publications*, 359(1), 115–  
447 133, doi:10.1144/SP359.7, 2011.
- 448 Trepmann, C. A. and Stöckhert, B.: Cataclastic deformation of garnet: a record of synseismic loading  
449 and postseismic creep, *Journal of Structural Geology*, 24(11), 1845–1856, doi:10.1016/S0191-  
450 8141(02)00004-4, 2002.
- 451 Voegelé, V., Cordier, P., Sautter, V., Sharp, T. G., Lardeaux, J. M. and Marques, F. O.: Plastic  
452 deformation of silicate garnets, *Physics of the Earth and Planetary Interiors*, 108(4), 319–338,  
453 doi:10.1016/S0031-9201(98)00111-3, 1998.
- 454 Vollbrecht, A., Pawlowski, J., Leiss, B., Heinrichs, T., Seidel, M. and Kronz, A.: Ductile deformation of  
455 garnet in mylonitic gneisses from the Münchberg Massif (Germany), *Tectonophysics*, 427(1–4), 153–  
456 170, doi:10.1016/j.tecto.2006.05.024, 2006.
- 457 Wang, Z. and Ji, S.: Deformation of silicate garnets; brittle-ductile transition and its geological  
458 implications, *The Canadian Mineralogist*, 37(2), 525, 1999.
- 459 Wayte, G. J., Worden, R. H., Rubie, D. C. and Droop, G. T. R.: A TEM study of disequilibrium  
460 plagioclase breakdown at high pressure: the role of infiltrating fluid, *Contributions to Mineralogy  
461 and Petrology*, 101(4), 426–437, doi:10.1007/BF00372216, 1989.
- 462 Wex, S., Mancktelow, N. S., Hawemann, F., Camacho, A. and Pennacchioni, G.: Geometry of a large-  
463 scale, low-angle, mid-crustal thrust (Woodroffe Thrust, central Australia): Geometry of a mid-crustal  
464 thrust, *Tectonics*, doi:10.1002/2017TC004681, 2017.
- 465 Wex, S., Mancktelow, N. S., Hawemann, F., Camacho, A. and Pennacchioni, G.: Inverted distribution  
466 of ductile deformation in the relatively “dry” middle crust across the Woodroffe Thrust, central  
467 Australia, *Solid Earth*, 9(4), 859–878, doi:10.5194/se-9-859-2018, 2018.
- 468 Wex, S., Mancktelow, N. S., Camacho, A. and Pennacchioni, G.: Interplay between seismic fracture  
469 and aseismic creep in the Woodroffe Thrust, central Australia – Inferences for the rheology of  
470 relatively dry continental mid-crustal levels, *Tectonophysics*, 758, 55–72,  
471 doi:10.1016/j.tecto.2018.10.024, 2019.
- 472
- 473
- 474
- 475
- 476
- 477
- 478



479 **Appendix**



481 *Figure A1: Thin section image in plane polarized light of a garnet crystal with monazite*  
482 *inclusions (with halos) and rutile-exsolution needles. b) BSE-image of the area indicated with*  
483 *the red box.*





485 *Figure A2: a) Misorientation map-detail for Fig. 6b), with b) pole figure plots for garnet axis*  
486 *with the same color scheme. The plots reveal a rotation around a (101)-axis, as indicated by*  
487 *the red circle.*